



Universiteit
Leiden
The Netherlands

Spatially resolved molecular interstellar medium in a $z = 6.6$ quasar host galaxy

Li, J.; Venemans, B.P.; Walter, F.; Decarli, R.; Wang, R.; Cai, Z.

Citation







Li, J., Venemans, B. P., Walter, F., Decarli, R., Wang, R., & Cai, Z. (2022). Spatially resolved molecular interstellar medium in a $z = 6.6$ quasar host galaxy. *The Astrophysical Journal*, 930(1). doi:10.3847/1538-4357/ac61d7

Version: Publisher's Version
License: [Creative Commons CC BY 4.0 license](https://creativecommons.org/licenses/by/4.0/)
Downloaded from: <https://hdl.handle.net/1887/3515596>

Note: To cite this publication please use the final published version (if applicable).



Spatially Resolved Molecular Interstellar Medium in a $z = 6.6$ Quasar Host Galaxy

Jianan Li^{1,2} , Bram P. Venemans^{3,4} , Fabian Walter^{3,5} , Roberto Decarli⁶ , Ran Wang¹ , and Zheng Cai² ¹Kavli Institute for Astronomy and Astrophysics, Peking University, Beijing 100871, People's Republic of China; jiananl@pku.edu.cn²Department of Astronomy, Tsinghua University, Beijing 100084, People's Republic of China³Max Planck Institute for Astronomy, Königstuhl 17, D-69117 Heidelberg, Germany⁴Leiden Observatory, Leiden University, P.O. Box 9513, 2300 RA Leiden, The Netherlands⁵National Radio Astronomy Observatory, Pete V. Domenici Array Science Center, P.O. Box O, Socorro, NM 87801, USA⁶INAF—Osservatorio di Astrofisica e Scienza dello Spazio, via Gobetti 93/3, I-40129 Bologna, Italy

Received 2021 November 3; revised 2022 March 23; accepted 2022 March 26; published 2022 May 2

Abstract

We present high spatial resolution ($\sim 0''.4$, 2.2 kpc) observations of the CO(6–5), CO(7–6), and [C I]_{369 μ m} lines and dust continuum emission from the interstellar medium (ISM) in the host galaxy of the quasar J0305–3150 at $z = 6.6$. These, together with archival [C II]_{158 μ m} data at a comparable spatial resolution, enable studies of the spatial distribution and kinematics between the ISM in different phases. When comparing the radial profiles of CO, [C II]_{158 μ m}, and the dust continuum, we find that the CO and dust continuum exhibit similar spatial distributions, both of which are less extended than the [C II]_{158 μ m}, indicating that the CO and dust continuum are tracing the same gas component, while the [C II]_{158 μ m} is tracing a more extended one. In addition, we derive the radial profiles of the [C II]_{158 μ m}/CO, [C II]_{158 μ m}/far-infrared (FIR), CO/FIR, and dust continuum $S_{98.7 \text{ GHz}}/S_{258.1 \text{ GHz}}$ ratios. We find a decreasing $S_{98.7 \text{ GHz}}/S_{258.1 \text{ GHz}}$ ratio with radius, possibly indicating a decrease of dust optical depth with increasing radius. We also detect some of the ISM lines and continuum emission in the companion galaxies previously discovered in the field around J0305–3150. Through comparing the line-to-line and line-to-FIR ratios, we find no significant differences between the quasar and its companion galaxies.

Unified Astronomy Thesaurus concepts: [Interstellar medium \(847\)](#); [Quasars \(1319\)](#); [Submillimeter astronomy \(1647\)](#); [AGN host galaxies \(2017\)](#); [Interstellar dust \(836\)](#); [High-redshift galaxies \(734\)](#); [Early universe \(435\)](#); [Molecular gas \(1073\)](#); [Interstellar atomic gas \(833\)](#)

1. Introduction

In the past two decades, the Atacama Large Millimeter/submillimeter Array (ALMA), the Northern Extended Millimeter Array (NOEMA), and the Karl G. Jansky Very Large Array (JVLA) have revealed detections of the (sub)millimeter dust and multiphase gas emission in quasar host galaxies in the early universe. Bright CO and [C II]_{158 μ m} emission lines are now frequently detected in the host galaxies of the quasars at the highest redshift. The majority of these observations are executed at $\gtrsim 0''.5$ spatial resolution, which trace the global interstellar medium (ISM) properties of these $z \gtrsim 6$ quasars (e.g., Wang et al. 2013, 2016; Decarli et al. 2018; Yang et al. 2019; Li et al. 2020a, 2020b). Spatially resolved ISM observations of $z \gtrsim 6$ quasars are only available for the brightest ISM emission lines, e.g., the [C II]_{158 μ m} line. These already reveal diversity of gas kinematics in the $z \gtrsim 6$ quasars, i.e., some of them suggest ordered rotation, while others show complex gas kinematics with no clear velocity gradient (e.g., Shao et al. 2017; Neeleman et al. 2019, 2021; Venemans et al. 2019, 2020; Wang et al. 2019b; Novak et al. 2020). Recently, spatially resolved CO observations at a spatial resolution of $\sim 0''.2$ for a $z = 6.327$ quasar have been obtained by Wang et al. (2019a), where they found a more concentrated spatial distribution of CO compared to the [C II]_{158 μ m} line.

Taking advantage of the high sensitivity of ALMA, a number of companion galaxies have recently been discovered

in the field of quasars at $z \gtrsim 6$ (e.g., Decarli et al. 2017, 2018; Venemans et al. 2018, 2020; Walter et al. 2018; Mazzucchelli et al. 2019; Neeleman et al. 2019, 2021). These companion galaxies are detected within $\lesssim 60$ kpc and within $\sim 1000 \text{ km s}^{-1}$ of the quasar redshift and are often found to be bright in the far-infrared (FIR; 42.5 \sim 122.5 μ m) continuum and the [C II]_{158 μ m} line. The brightest ones have [C II]_{158 μ m} luminosities comparable to or even brighter than those of the quasar host galaxies, while the less luminous companions are over an order of magnitude fainter. Direct comparisons of the quasar with their companion galaxies provide a unique view on the potential impact of the active galactic nuclei (AGNs) on the ISM properties. Observations of fine structure lines and molecular CO suggest similar [O III]_{88 μ m}/FIR and [C II]_{158 μ m}/FIR ratios but different CO excitation between the quasars and their companions (e.g., Walter et al. 2018; Neeleman et al. 2019; Pensabene et al. 2021).

The quasar VIKING J030516.92–315056.0 (hereafter J0305–3150) is among the FIR brightest quasars at $z > 6$ with a FIR luminosity of $(1.60 \pm 0.06) \times 10^{13} L_{\odot}$ (Venemans et al. 2019). It was also detected in the [C II]_{158 μ m} line with a luminosity of $(5.9 \pm 0.4) \times 10^9 L_{\odot}$ (Venemans et al. 2019). In ALMA Cycle 2, Venemans et al. (2017) detected the CO(6–5) and CO(7–6) lines. ALMA observations of the [C II]_{158 μ m} line with extremely high spatial resolution ($0''.076$, 410 pc) were reported in Venemans et al. (2019), which reveal complex gas spatial distribution and kinematics. Two cavities found in the zero velocity channel map as well as the intensity map suggest that the quasar is likely to affect the spatial distribution and kinematics of its surrounding ISM in the host galaxy. In addition, three companion galaxies within 40 kpc from the quasar J0305–3150 were detected in [C II]_{158 μ m}.



In this paper, we present spatially resolved ($\sim 0''.4$, 2.2 kpc) ALMA observations of the CO(6–5), CO(7–6), and [C I] $_{369\ \mu\text{m}}$ emission lines as well as the dust continuum emission of the quasar J0305–3150. These observations probe the molecular ISM, and enable a direct comparison of the spatial distribution and kinematics of the ISM emission in different phases, when combined with previous [C II] $_{158\ \mu\text{m}}$ observations at a similar spatial resolution. In addition, comparisons of the quasar emission with that of the companion galaxies will enable a study of the impact of the AGN on the gas properties. We adopt a standard Λ CDM cosmology with $H_0 = 70\ \text{km s}^{-1}\ \text{Mpc}^{-1}$ and $\Omega_m = 0.3$, throughout this paper.

2. Observations

We obtained ALMA observations of the CO(6–5), CO(7–6), and [C I] $_{369\ \mu\text{m}}$ emission lines as well as the underlying continuum of J0305–3150 during 2017 December 4–17 (Cycle 5 program ID 2017.1.01532.S). 45–47 antennas were used in the C43–6 configuration and the baseline length was between 15 and 2517 m. The total observing time was 3.67 hr on source. J2357–5311 was used for flux and bandpass calibration, and the phase calibrator was J0326–3243. The ALMA Band 3 receiver covered the CO(6–5) line in the lower sideband and the CO(7–6) and [C I] $_{369\ \mu\text{m}}$ lines in the upper sideband, while the remaining two spectral windows were observing the continuum emission.

To study the spatial distribution and kinematics of the ISM in different phases, we also use earlier ALMA data of the [C II] $_{158\ \mu\text{m}}$ line, which trace the neutral ISM (Cycle 3 program ID 2015.1.00399.S). These [C II] $_{158\ \mu\text{m}}$ data of J0305–3150 have previously been published in Venemans et al. (2020).

All the data were reduced following the standard pipeline and imaged using the TCLEAN task in CASA. To obtain a comparable beam size of the [C II] $_{158\ \mu\text{m}}$ with that of the CO lines, we employed natural weighting for the [C II] $_{158\ \mu\text{m}}$ data and Briggs weighting with a robust parameter of 0.5 for the CO lines in imaging. This leads to synthesized beam sizes of $0''.20 \times 0''.20$ for [C II] $_{158\ \mu\text{m}}$, $0''.44 \times 0''.30$ for CO(6–5), and $0''.37 \times 0''.26$ for CO(7–6) and [C I] $_{369\ \mu\text{m}}$ in FWHM. To match the beam sizes of CO and [C II] $_{158\ \mu\text{m}}$, we downgraded the spatial resolution of the [C II] $_{158\ \mu\text{m}}$ data to that of the CO(6–5) line using the convolve2D function in CASA. We used all line-free channels to image the continuum. A first-order polynomial continuum was subtracted from the data cube using the UVCONTSUB task in CASA for spectral line imaging. We binned the [C II] $_{158\ \mu\text{m}}$ line to $35\ \text{km s}^{-1}$ width and the resulting rms was $0.28\ \text{mJy beam}^{-1}$ per binned channel. The CO(6–5), CO(7–6), and [C I] $_{369\ \mu\text{m}}$ lines were also binned to $35\ \text{km s}^{-1}$ width and the rms was $0.13\ \text{mJy beam}^{-1}$ per binned channel. All line-free channels were used for the continuum imaging. The continuum sensitivities were 5.7 and $20.3\ \mu\text{Jy beam}^{-1}$ at 98.7 and 258.1 GHz, respectively.

3. Results

3.1. The Quasar

We detect the CO(6–5), CO(7–6), and [C I] $_{369\ \mu\text{m}}$ emission lines, as well as the underlying continuum emission of the quasar J0305–3150. All the spectral lines and the continuum emission are spatially resolved at our resolution of $\sim 0''.4$. We show the intensity, velocity, and velocity dispersion maps in

Figure 1. The beam-matched [C II] $_{158\ \mu\text{m}}$ data is shown as well for comparison (Venemans et al. 2020). We find a part with high velocity and high velocity dispersion northeast to the quasar on the CO and [C II] $_{158\ \mu\text{m}}$ maps. This position is coincident with the peak of the companion galaxy C1 discovered in Venemans et al. (2019). The high velocity/velocity dispersion in that region is likely a result of interactions between the quasar and C1. The velocity and velocity dispersion maps of all the spectral lines reveal some rotation and high velocity dispersion, which is consistent with results obtained for the superhigh resolution [C II] $_{158\ \mu\text{m}}$ data (Venemans et al. 2019). We measure the source sizes of the emission lines and the continuum emissions through the CASA UVMODELFIT task in the UV plane. This leads to a comparable source size of $(0.39 \pm 0.04) \times (0.32 \pm 0.04)$ with a position angle (PA) of $\text{PA} = 109^\circ \pm 75^\circ$ for the CO(6–5) line, and $(0.32 \pm 0.03) \times (0.26 \pm 0.03)$, $\text{PA} = -68^\circ \pm 20^\circ$ for the CO(7–6) line. The [C II] $_{158\ \mu\text{m}}$ line suggests a larger source size of $(0.51 \pm 0.02) \times (0.47 \pm 0.02)$, $\text{PA} = 127^\circ \pm 28^\circ$. The deconvolved size for the continuum emission at 98.7 GHz is $(0.30 \pm 0.01) \times (0.28 \pm 0.01)$, $\text{PA} = 9^\circ \pm 43^\circ$.

We measure the spectral line fluxes within an aperture of $0''.75$ with the residual scaling method presented in Novak et al. (2019), to obtain emission of the quasar while avoiding possible contaminations from the close companion C1. The resulting spectra are shown in Figure 2. As the [C I] $_{369\ \mu\text{m}}$ emission line is not as strong as the CO lines, we assume the same line width for the CO and the [C I] $_{369\ \mu\text{m}}$ lines and fit the three lines, namely CO(6–5), CO(7–6), and [C I] $_{369\ \mu\text{m}}$, simultaneously with three Gaussians. This leads to a line width of $250 \pm 11\ \text{km s}^{-1}$ in FWHM, and line fluxes of 0.63 ± 0.04 , 0.55 ± 0.04 , and $0.25 \pm 0.03\ \text{Jy km s}^{-1}$ for the CO(6–5), CO(7–6), and [C I] $_{369\ \mu\text{m}}$ lines, respectively. The derived CO(6–5) and CO(7–6) line fluxes are consistent with results obtained in ALMA Cycle 2 observations within the uncertainties (Venemans et al. 2017). We fit the spectrum of the [C II] $_{158\ \mu\text{m}}$ line with a Gaussian profile. This yields a line width of $268 \pm 11\ \text{km s}^{-1}$ in FWHM, and a line flux of $5.25 \pm 0.30\ \text{Jy km s}^{-1}$. The derived line widths for the [C II] $_{158\ \mu\text{m}}$, CO, and [C I] $_{369\ \mu\text{m}}$ lines are consistent within the uncertainties. The measured [C II] $_{158\ \mu\text{m}}$ flux is consistent with that obtained in Venemans et al. (2019, 2020). The measured line widths, fluxes, and luminosities are listed in Table 1. The continuum flux densities measured within the aperture are 0.27 ± 0.02 and $5.20 \pm 0.08\ \text{mJy}$ at 98.7 and 258.1 GHz, respectively.

3.2. Companion Galaxies

Our reanalysis of the [C II] $_{158\ \mu\text{m}}$ data confirms the three companion sources originally reported in Venemans et al. (2019). In addition, we detect the CO(6–5) or/and CO(7–6) lines in some of the companion galaxies (namely C1, C2, and C3). The [C II] $_{158\ \mu\text{m}}$, [C I] $_{369\ \mu\text{m}}$, CO(6–5), and CO(7–6) intensity maps of C1, C2, and C3 are shown in Figure 3. The spectral line fluxes for companion galaxies are measured in intensity maps through adopting line widths determined from superhigh resolution [C II] $_{158\ \mu\text{m}}$ data (Venemans et al. 2019). We detect the [C II] $_{158\ \mu\text{m}}$ and CO(6–5) lines in C1. We do not detect the CO(7–6) line, possibly because of a low signal-to-noise ratio (S/N) at that frequency. Considering its close distance to the quasar, we measure the line flux within a $0''.3$ radius aperture centered on the [C II] $_{158\ \mu\text{m}}$ peak. The resulting line fluxes are 0.06 ± 0.01 and $0.48 \pm 0.03\ \text{Jy km s}^{-1}$ for CO(6–5) and [C II] $_{158\ \mu\text{m}}$. The 3σ upper limits for CO(7–6)

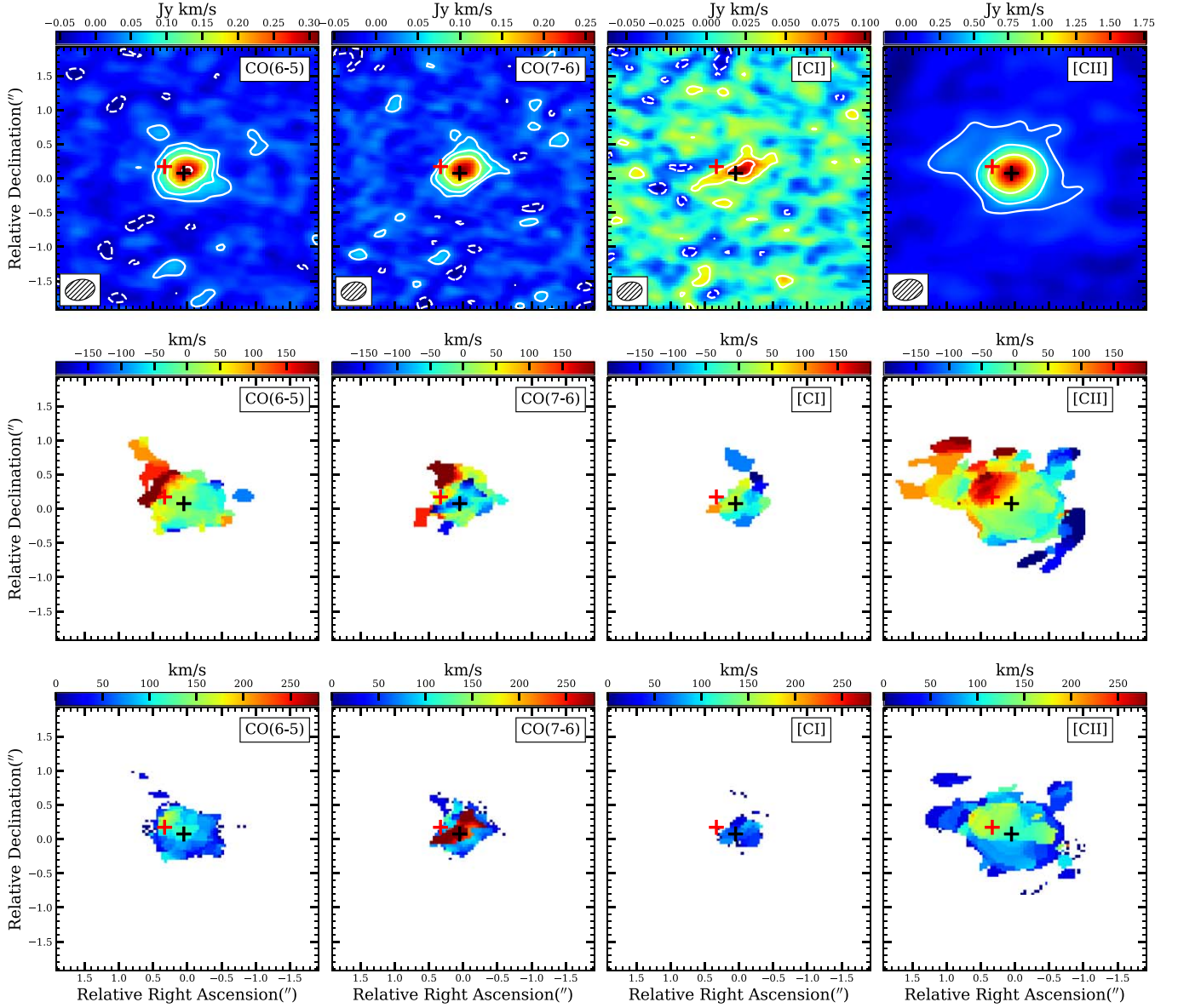


Figure 1. Line intensity, velocity, and velocity dispersion maps (from top to bottom) of the quasar J0305–3150. The white contours are $[-2, 2, 4, 8, 16] \times \sigma$, $\sigma = 0.018 \text{ Jy km s}^{-1}$ for the CO(6–5) line, $[-2, 2, 4, 8, 16] \times \sigma$, $\sigma = 0.017 \text{ Jy km s}^{-1}$ for the CO(7–6) line, $[-2, 2, 4] \times \sigma$, $\sigma = 0.020 \text{ Jy km s}^{-1}$ for the [C I] $_{369 \mu\text{m}}$ line, and $[-2, 2, 4, 8] \times \sigma$, $\sigma = 0.051 \text{ Jy km s}^{-1}$ for the [C II] $_{158 \mu\text{m}}$ line. The white ellipse on the lower left represents the size of the beam. The beam sizes from left to right are $0''.44 \times 0''.30$, PA = -77.00 deg, $0''.37 \times 0''.26$, PA = -74.92 deg, $0''.37 \times 0''.26$, PA = -74.90 deg, and $0''.44 \times 0''.30$, PA = -77.00 deg. For the velocity and velocity dispersion maps, all the pixels with S/N > 2 are included. The black and red crosses represent the [C II] $_{158 \mu\text{m}}$ peak position for the quasar and C1, respectively.

and [C I] $_{369 \mu\text{m}}$ are both $0.04 \text{ Jy km s}^{-1}$. C2 is only detected in the [C II] $_{158 \mu\text{m}}$ line with a line flux of $0.27 \pm 0.07 \text{ Jy km s}^{-1}$, leaving 3σ upper limits of 0.05, 0.04, and $0.04 \text{ Jy km s}^{-1}$ for CO(6–5), CO(7–6), and [C I] $_{369 \mu\text{m}}$. As for C3, the [C II] $_{158 \mu\text{m}}$ intensity map suggests an extended gas structure, while the CO(6–5) and CO(7–6) emissions are not spatially resolved. The extended [C II] $_{158 \mu\text{m}}$ feature is also observed in the superhigh resolution [C II] $_{158 \mu\text{m}}$ data (Venemans et al. 2019). The CO(6–5) and CO(7–6) fluxes of C3 are 0.05 ± 0.02 and $0.07 \pm 0.02 \text{ Jy km s}^{-1}$. The [C I] $_{369 \mu\text{m}}$ flux upper limit for C3 is $0.05 \text{ Jy km s}^{-1}$. The measured [C II] $_{158 \mu\text{m}}$ fluxes for the three companion galaxies are consistent with those obtained in the high spatial resolution observations (Venemans et al. 2019). We show the spectra of [C II] $_{158 \mu\text{m}}$ for the companion galaxies in Figure 2. As for the

continuum detections, only C3 has been detected in the 258.1 GHz continuum, leaving a continuum flux density of $0.44 \pm 0.08 \text{ mJy}$. Through combining observations in different ALMA cycles, Venemans et al. (2020) detect the 258.1 GHz continuum emission in all the three companion galaxies around J0305–3150. The nondetection of the C2 continuum at 258.1 GHz thus suggests that the 3σ limit of the emission surface brightness is $16.0 \mu\text{Jy kpc}^{-2}$. The 3σ upper limits for the surface brightness for C2 and C3 at 98.7 GHz are both $1.5 \mu\text{Jy kpc}^{-2}$. In Figure 4, we show the continuum maps at 98.7 and 258.1 GHz. The peak positions of the [C II] $_{158 \mu\text{m}}$ line and the 258.1 GHz continuum for C3 are consistent. Details of the quasar and the companion galaxy measurements are listed in Table 1.

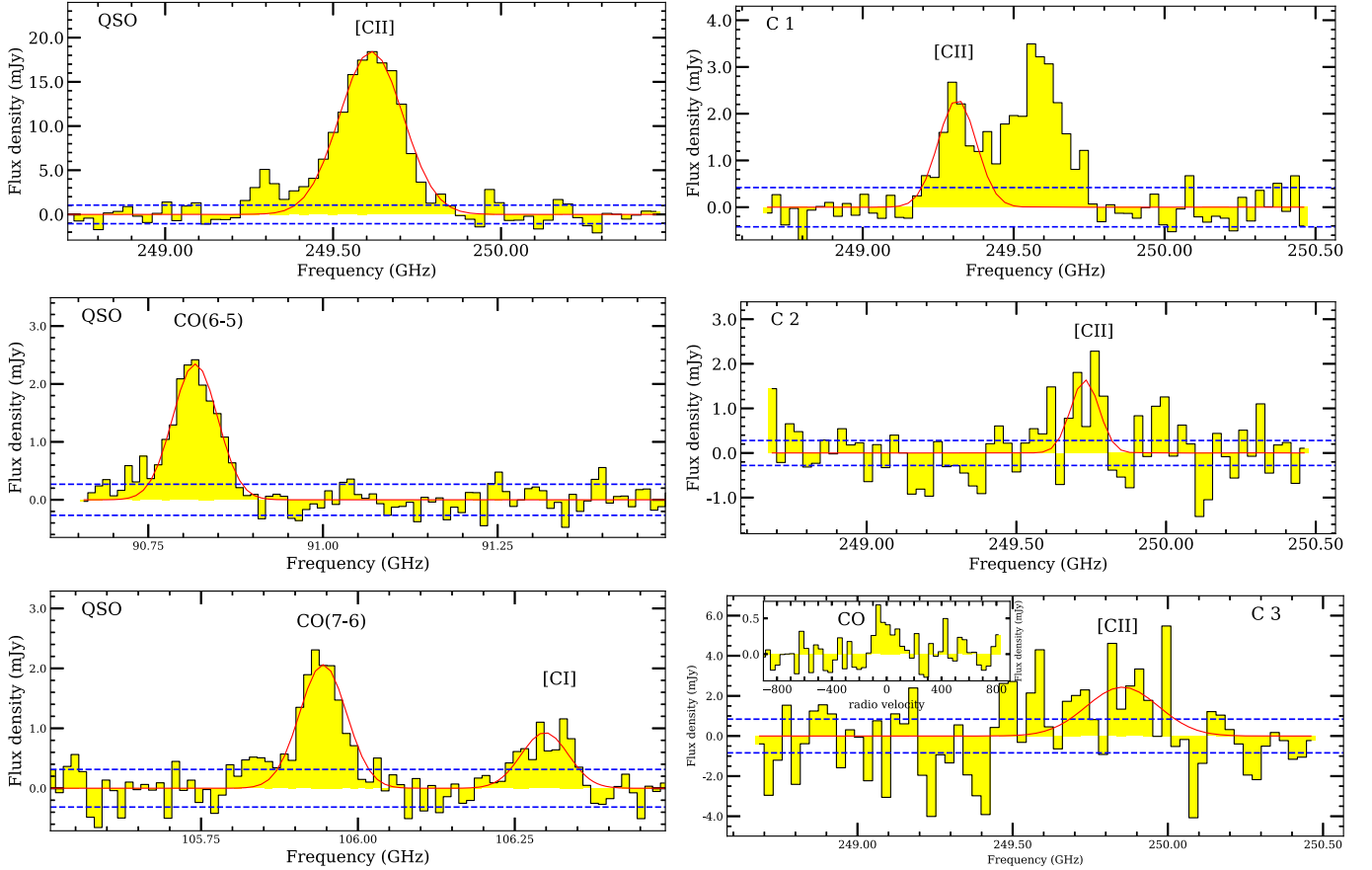


Figure 2. Left column: spectra of $[\text{C II}]_{158 \mu\text{m}}$, $\text{CO}(6-5)$, and $\text{CO}(7-6)$ for the quasar J0305–3150. Data are shown in yellow histograms. The red solid lines are Gaussian profile fits to the spectra with the line centers fixed to the $[\text{C II}]_{158 \mu\text{m}}$ redshift of $z = 6.61391$ (Venemans et al. 2019). The continuum has been subtracted for each of the spectra here displayed. Right column: $[\text{C II}]_{158 \mu\text{m}}$ spectra for the companion galaxies C1, C2, and C3. Data are shown in yellow histograms. The red solid lines are Gaussian profile fits to the spectra with the line centers fixed to the $[\text{C II}]_{158 \mu\text{m}}$ redshift obtained from Venemans et al. (2019). The blue dashed lines indicate the noise at $\pm 1\sigma$ level. The $[\text{C II}]_{158 \mu\text{m}}$ spectrum of C3 is extracted from an aperture with a radius of $0''.6$. The spectral channel widths for the quasar and the companion galaxies are 35 km s^{-1} . For the source C3, we present a stacked spectrum of the $\text{CO}(7-6)$ and $\text{CO}(6-5)$ lines extracted from the peak positions on the top left of the $[\text{C II}]_{158 \mu\text{m}}$ spectrum panel.

4. Discussion

4.1. Spatial Distribution and Resolved Ratios of Different Gas Tracers

We study the dependence of the spectral line and the continuum intensities with distances to the quasar, to explore the spatial distribution of the gas in different phases and the dust. To obtain the radial profiles, we divide the intensity maps into a series of concentric rings with a width of $0''.1$, with the center fixed to the peak flux pixel, and the major and minor axes and the position angle fixed to the parameters adopted from the $[\text{C II}]_{158 \mu\text{m}}$ source size. To increase the S/N of the CO measurements, we take the average of the $\text{CO}(6-5)$ and $\text{CO}(7-6)$ data cubes to form a mean CO intensity map. The resulting radial profiles are shown in Figure 5. All the lines and continuum show intensities that exceed the radial profile of the dirty beam ($0''.4$) at large radii, implying that the sources are extended. The radial profile of CO follows that of the continuum within the uncertainties, indicating that they are possibly originated from the same gas component. The $[\text{C II}]_{158 \mu\text{m}}$ radial profile reduces to half of the peak intensity at a larger radius compared to that of the CO and dust continuum, which implies that the $[\text{C II}]_{158 \mu\text{m}}$ emission is more extended than the CO and the continuum. This result is consistent with

previous findings that the $[\text{C II}]_{158 \mu\text{m}}$ line in $z \gtrsim 6$ quasars has larger source sizes than those of the mid- to high- J ($J \gtrsim 5$) CO and dust continuum (e.g., Shao et al. 2017; Li et al. 2020b; Venemans et al. 2020). As for low- J ($J \lesssim 3$) CO lines, Shao et al. (2019) find similar source sizes to that of $[\text{C II}]_{158 \mu\text{m}}$ in a sample of three $z \gtrsim 6$ quasars, while both of them are larger than the sizes of dust continuum.

In Figure 5, we also show the radial profiles of the $\text{CO}/[\text{C II}]_{158 \mu\text{m}}$, CO/FIR , and $[\text{C II}]_{158 \mu\text{m}}/\text{FIR}$ ratios as well as the continuum flux density ratio ($S_{98.7 \text{ GHz}}/S_{258.1 \text{ GHz}}$). Similar to findings in high resolution $[\text{C II}]_{158 \mu\text{m}}$ observations of other $z \gtrsim 6$ quasars, the $[\text{C II}]_{158 \mu\text{m}}/\text{FIR}$ ratio of J0305–3150 exhibits a deficit in the center and an increasing trend with increasing distance to the center. The CO/FIR ratio is almost flat with increasing radius. A decreasing trend of the $\text{CO}/[\text{C II}]_{158 \mu\text{m}}$ ratio with increasing radius is consistent with an extended spatial distribution of the $[\text{C II}]_{158 \mu\text{m}}$ line relative to CO assuming the spatial distribution of these two lines are Gaussian. Interestingly, we find a decreasing trend of the $S_{98.7 \text{ GHz}}/S_{258.1 \text{ GHz}}$ ratio with increasing radius.

The dust emission (S_ν) is described through

$$S_\nu \propto (1 - e^{-\tau_\nu})(B_\nu(T_{\text{dust}}) - B_\nu(T_{\text{CMB}})), \quad (1)$$

Table 1
Observational Results and Derived Properties of the Quasar J0305–3150 and Its Companion Galaxies

	J0305–3150	C1	C2	C3
R.A.	03 ^h 05 ^m 16 ^s .92	03 ^h 05 ^m 16 ^s .95	03 ^h 05 ^m 16 ^s .87	03 ^h 05 ^m 16 ^s .38
Decl.	−31°50′55″.92(6)	−31°50′55″.74(13)	−31°50′55″.26(23)	−31°50′54″.96(31)
$z_{[\text{C II}]}$	6.61391 ± 0.00015	6.6231 ± 0.0003	6.6104 ± 0.0004	6.6066 ± 0.0006
FWHM_{CO} (km s ^{−1})	250 ± 11			
CO(6–5) flux (Jy km s ^{−1})	0.63 ± 0.04	0.06 ± 0.01	<0.05	0.05 ± 0.02
$L_{\text{CO}(6-5)}$ ($\times 10^8 L_{\odot}$)	2.49 ± 0.16	0.25 ± 0.04	<0.18	0.20 ± 0.08
Deconvolved size (CO(6–5))	$(0.39 \pm 0.04) \times (0.32 \pm 0.04)$, PA = 109° ± 75°			
CO(7–6) flux (Jy km s ^{−1})	0.55 ± 0.04	<0.04	<0.04	0.07 ± 0.02
$L_{\text{CO}(7-6)}$ ($\times 10^8 L_{\odot}$)	2.53 ± 0.18	<0.19	<0.20	0.31 ± 0.08
Deconvolved size (CO(7–6))	$(0.32 \pm 0.03) \times (0.26 \pm 0.03)$, PA = −68° ± 20°			
[C I] _{369 μm} flux (Jy km s ^{−1})	0.25 ± 0.03	<0.04	<0.04	<0.05
$L_{[\text{C I}](2-1)}$ ($\times 10^8 L_{\odot}$)	1.15 ± 0.14	<0.19	<0.20	<0.22
$S_{258.1 \text{ GHz}}$ (mJy)	5.20 ± 0.08			0.44 ± 0.08
$S_{98.7 \text{ GHz}}$ (mJy)	0.27 ± 0.02			
Deconvolved size (98.7 GHz)	$(0.30 \pm 0.01) \times (0.28 \pm 0.01)$, PA = 9° ± 43°			
$\text{FWHM}_{[\text{C II}]}$ (Jy km s ^{−1})	268 ± 11			
[C II] _{158 μm} flux (Jy km s ^{−1})	5.25 ± 0.30	0.48 ± 0.03	0.27 ± 0.07	0.87 ± 0.31
$L_{[\text{C II}]}$ ($\times 10^8 L_{\odot}$)	56.94 ± 3.25	5.16 ± 0.33	2.93 ± 0.76	9.41 ± 3.36
Deconvolved size ^e ([C II])	$(0.51 \pm 0.02) \times (0.47 \pm 0.02)$, PA = 127° ± 28°			
$M_{\text{H}_2, \text{CO}}$ ($\times 10^{10} M_{\odot}$)	2.2–4.0	0.21–0.37	<0.36	0.24–0.44
$M_{\text{H}_2, [\text{C I}]}$ ($\times 10^{10} M_{\odot}$)	3.0 ± 1.3	<0.48	<0.44	<0.60
$\Sigma_{\text{H}_2, \text{CO}}$ ($M_{\odot} \text{ pc}^{-2}$)	$1.4\text{--}2.6 \times 10^4$	>213		>244
$\Sigma_{\text{H}_2, [\text{C I}]}$ ($M_{\odot} \text{ pc}^{-2}$)	$(2.0 \pm 0.9) \times 10^4$			

Note. The source positions are determined from the peak pixels in the [C II]_{158 μm} intensity maps. The astrometric uncertainties are given in milliarcseconds in parentheses. The [C II]_{158 μm} redshifts are adopted from Venemans et al. (2019). We assume the same line widths for the CO(6–5), CO(7–6), and [C I]_{369 μm} lines and fit the three lines together during the line flux measurements for the quasar, and the fitting result for the line width is given in FWHM_{CO} . The fluxes for the quasar are measured within an aperture with a radius of 0″.75. To avoid contamination from the quasar, the flux of C1 is measured from a 0″.3 radius aperture. We use a 0″.6 radius aperture to obtain the [C II]_{158 μm} fluxes of the C3 emission line and continuum. To calculate the gas surface densities of the companion galaxies, we assume the emission to be spatially unresolved and apply the beam sizes as upper limits for the source sizes.

where $B_{\nu}(T_{\text{dust}})$ and $B_{\nu}(T_{\text{CMB}})$ are the Planck function at dust temperature and cosmic microwave background temperature, respectively. τ_{ν} is optical depth, which can be further expressed as

$$\tau_{\nu} = \kappa_{\nu} \Sigma_{\text{dust}}. \quad (2)$$

κ_{ν} is dust opacity, which depends on frequency through

$$\kappa_{\nu} = \kappa_0 \left(\frac{\nu}{\nu_0} \right)^{\beta}, \quad (3)$$

and Σ_{dust} is dust mass surface density, which is independent on frequency. We consider two simplifications. In the first case we assume τ_{ν} remains constant with radius, but we enable T_{dust} as a function of radius (r). The derivatives of the dust continuum ratio ($S_{98.7 \text{ GHz}}/S_{258.1 \text{ GHz}}$) relative to r is

$$\frac{d(S_{98.7 \text{ GHz}}/S_{258.1 \text{ GHz}})}{d(r)} \propto -\frac{d(T_{\text{dust}}(r))}{d(r)}, \quad (4)$$

suggesting an opposite monotonicity of $S_{98.7 \text{ GHz}}/S_{258.1 \text{ GHz}}$ relative to $T_{\text{dust}}(r)$. In the second simplification, we assume a constant T_{dust} throughout the source, while considering τ_{ν} as a function of r (the r dependence of $\tau_{\nu}(r)$ reduces to $\Sigma_{\text{dust}}(r)$ through $\tau_{\nu}(r) = \kappa_0 \left(\frac{\nu}{\nu_0} \right)^{\beta} \times \Sigma_{\text{dust}}(r)$). The derivative of $S_{98.7 \text{ GHz}}/S_{258.1 \text{ GHz}}$ relative to r is

$$\frac{d(S_{98.7 \text{ GHz}}/S_{258.1 \text{ GHz}})}{d(r)} \propto \frac{d(\tau_{\nu}(r))}{d(r)} \propto \frac{d(\Sigma_{\text{dust}}(r))}{d(r)}, \quad (5)$$

indicating the same monotonicity between $S_{98.7 \text{ GHz}}/S_{258.1 \text{ GHz}}$ and $\tau_{\nu}(r)$ (or $\Sigma_{\text{dust}}(r)$). Accordingly, the decreasing $S_{98.7 \text{ GHz}}/S_{258.1 \text{ GHz}}$ ratio with increasing radius can be explained by (1) an increase of $T_{\text{dust}}(r)$ with r assuming a uniform τ_{ν} or (2) a decrease of $\tau_{\nu}(r)$ or $\Sigma_{\text{dust}}(r)$ with r for constant T_{dust} across r . An increasing temperature with increasing radius seems inconsistent with the scenario of more AGN dust heating toward the center. However, we cannot rule out that the interactions between the quasar and C1 drive the observed increasing temperature with increasing distances to the center. The second explanation is more likely to be the case, given that decreasing Σ_{dust} (or $\tau_{\nu}(r)$) with radius is expected.

4.2. Gas Properties

We estimate the molecular gas mass of the quasar based on the CO and [C I]_{369 μm} lines. Assuming the [C I]_{369 μm} emission to be optically thin, the neutral carbon mass can be estimated through

$$\frac{M_{\text{C}}}{M_{\odot}} = 4.566 \times 10^{-4} \frac{Q(T_{\text{ex}})}{5} \times e^{62.5/T_{\text{ex}}} \frac{L'_{[\text{C I}]}}{\text{K km s}^{-1} \text{ pc}^{-2}}, \quad (6)$$

where $Q(T_{\text{ex}}) = 1 + 3e^{-23.6/T_{\text{ex}}} + 5e^{-62.5/T_{\text{ex}}}$ is the partition function and T_{ex} is the excitation temperature (Weiß et al. 2003, 2005; Venemans et al. 2017). Adopting $T_{\text{ex}} = 30 \text{ K}$ from

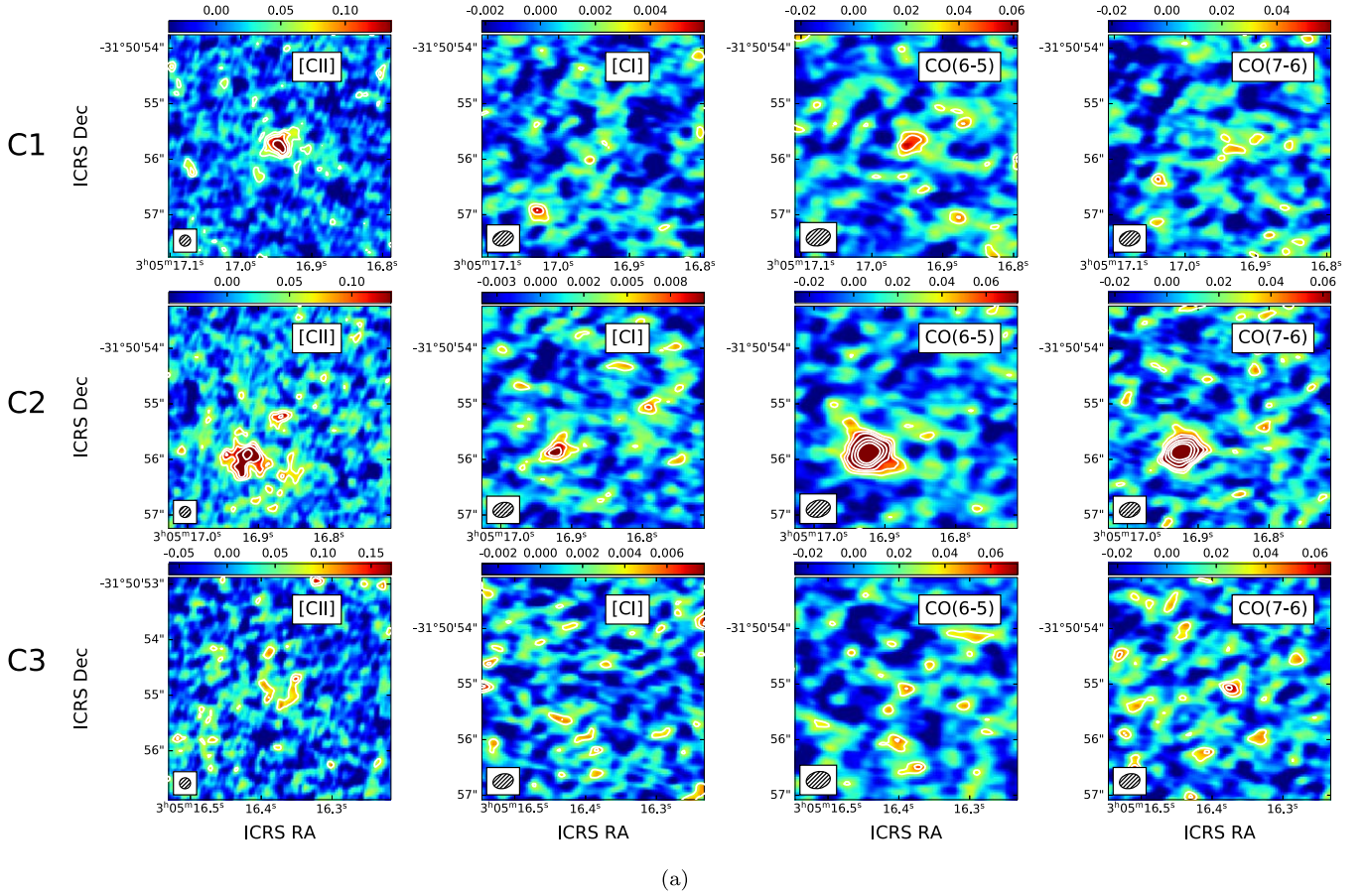


Figure 3. [C II] $_{158\ \mu\text{m}}$, [C I] $_{369\ \mu\text{m}}$, CO(6–5), and CO(7–6) intensity maps (from left to right) centered on the companion galaxies C1, C2, and C3 (from top to bottom). The beam is shown on the bottom left. Black contours on the C1 intensity maps are $[-2, 2, 3, 4] \times \sigma$ ($\sigma = 0.024\ \text{Jy km s}^{-1}$), $[-2, 2] \times \sigma$ ($\sigma = 0.012\ \text{Jy km s}^{-1}$), $[-2, 2, 3] \times \sigma$ ($\sigma = 0.012\ \text{Jy km s}^{-1}$), and $[-2, 2] \times \sigma$ ($\sigma = 0.011\ \text{Jy km s}^{-1}$) from left to right. Contours on the C2 maps are $[-2, 2, 3, 4] \times \sigma$ ($\sigma = 0.031\ \text{Jy km s}^{-1}$), $[-2, 2] \times \sigma$ ($\sigma = 0.012\ \text{Jy km s}^{-1}$), $[-2, 2] \times \sigma$ ($\sigma = 0.013\ \text{Jy km s}^{-1}$), and $[-2, 2] \times \sigma$ ($\sigma = 0.010\ \text{Jy km s}^{-1}$) from left to right. As for C3, black contours are $[-2, 2, 3, 4] \times \sigma$ ($\sigma = 0.041\ \text{Jy km s}^{-1}$), $[-2, 2] \times \sigma$ ($\sigma = 0.012\ \text{Jy km s}^{-1}$), $[-2, 2, 3] \times \sigma$ ($\sigma = 0.016\ \text{Jy km s}^{-1}$), and $[-2, 2, 3, 4] \times \sigma$ ($\sigma = 0.017\ \text{Jy km s}^{-1}$) from left to right.

Venemans et al. (2017), we estimate a neutral carbon mass of $M_{[\text{C I}]} = (1.5 \pm 0.2) \times 10^7 M_{\odot}$ based on the [C I] $_{369\ \mu\text{m}}$ line. The neutral carbon abundance relative to molecular hydrogen is $X_{[\text{C I}]} = M_{[\text{C I}]} / (6 M_{\text{H}_2})$. Utilizing the neutral carbon abundance measured in $z = 2\text{--}3$ infrared bright galaxies from Walter et al. (2011) of $X_{[\text{C I}]} = (8.4 \pm 3.5) \times 10^{-5}$, we estimate a molecular gas mass of $(3.0 \pm 1.3) \times 10^{10} M_{\odot}$. We derive a molecular gas mass surface density of $(2.0 \pm 0.9) \times 10^4 M_{\odot} \text{pc}^{-2}$. We also estimate the molecular gas masses for the three companion galaxies based on their [C I] $_{369\ \mu\text{m}}$ upper limits. The resulting 3σ upper limits for the molecular gas masses of C1, C2, and C3 are $<4.8 \times 10^9 M_{\odot}$, $<4.4 \times 10^9 M_{\odot}$, and $<6.0 \times 10^9 M_{\odot}$, respectively.

Low- J CO transitions trace the cold molecular gas, and thus can be used as molecular gas mass indicators through

$$M_{\text{H}_2} = \alpha_{\text{CO}} \times L'_{\text{CO}}, \quad (7)$$

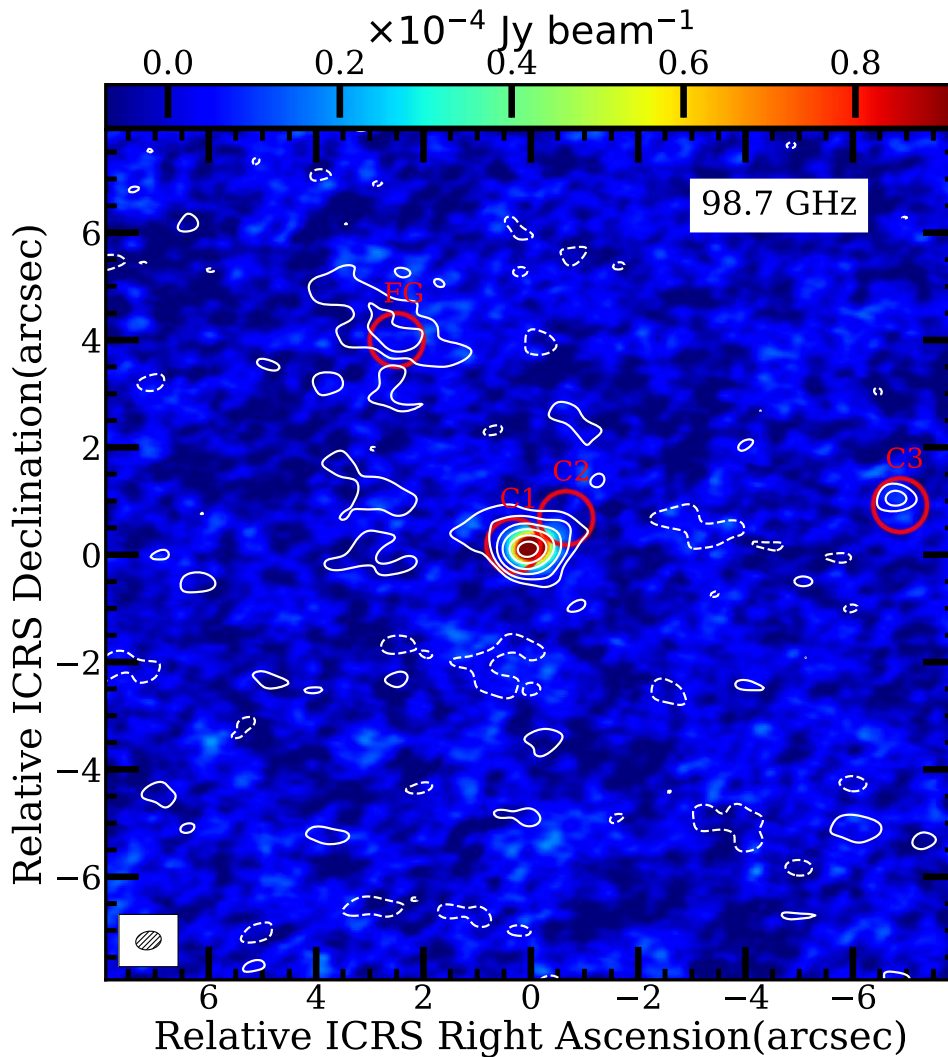
where α_{CO} is the molecular gas conversion factor, and L'_{CO} is the CO luminosity in the unit of $\text{K km s}^{-1} \text{pc}^2$. L'_{CO} is calculated from the CO flux $S_{\text{CO}} \delta \nu$ through

$$L'_{\text{CO}} = 3.25 \times 10^7 S_{\text{CO}} \delta \nu \frac{D_L^2}{(1+z)^3 \nu_{\text{obs}}^2}. \quad (8)$$

For J0305–3150, we only detect the CO(6–5) and CO(7–6) lines. To derive molecular gas mass, we utilize the following

two methods to estimate the CO(1–0) flux from the CO(6–5) line. (1) We employ the CO(6–5)/CO(1–0) ratio of the CO spectral line energy distribution model prediction for J2310+1855 (Li et al. 2020b); this leads to an estimated molecular gas mass of $(2.70 \pm 0.17) \times 10^{10} M_{\odot}$. (2) We use the observed CO(6–5)/CO(2–1) flux ratio in the range of 5.7–10.3 for $z \gtrsim 6$ quasars in Shao et al. (2019). Using the approximation that $L'_{\text{CO}(2-1)} \approx L'_{\text{CO}(1-0)}$ from Carilli & Walter (2013), and adopting a conversion factor for local (ultra)luminous infrared galaxies ((U)LIRGs) of $\alpha_{\text{CO}} = 0.8 M_{\odot} (\text{K km s}^{-1} \text{pc}^2)^{-1}$ (Downes & Solomon 1998), we estimate the molecular gas mass of J0305–3150 from the CO lines to be $2.2\text{--}4.0 \times 10^{10} M_{\odot}$. The derived molecular gas mass surface density is $1.4\text{--}2.6 \times 10^4 M_{\odot} \text{pc}^{-2}$. As for the companion galaxies, the molecular gas masses based on CO are $2.1\text{--}3.7 \times 10^9 M_{\odot}$, $<3.6 \times 10^9 M_{\odot}$, and $2.4\text{--}4.4 \times 10^9 M_{\odot}$ for C1, C2, and C3, respectively. Assuming the CO lines of companion galaxies are spatially unresolved, we thus estimate the 3σ lower limit of the gas mass surface density to be $>213 M_{\odot} \text{pc}^{-2}$ and $>244 M_{\odot} \text{pc}^{-2}$ for C1 and C3, respectively.

The gas masses based on CO and [C I] $_{369\ \mu\text{m}}$ are within the uncertainties. In Figure 6, we show the relation between the star formation rate density and molecular gas surface density for J0305–3150 and the companion galaxies. The derived molecular gas



(a)

Figure 4. Colors represent continuum at 98.7 GHz. White contours: beam-matched continuum at 258.1 GHz with levels of $[-2, 2, 4, 8, 16, 32, 55] \times \sigma$ ($\sigma = 23.8 \mu\text{Jy beam}^{-1}$). Positions of the companion galaxies are shown as red circles. “FG” represents the foreground source reported in Figure 6 of Venemans et al. (2019).

mass surface densities of the quasar from both CO and $[\text{C I}]_{369 \mu\text{m}}$ are consistent and comparable to the maximum values found in local starburst galaxies (Kennicutt & De Los Reyes 2021). The gas surface density 3σ upper limits for C3 are consistent with the lowest value found for the average of local starburst galaxies, and higher than the lowest value found for the average of local spiral galaxies (de los Reyes & Kennicutt 2019; Kennicutt & De Los Reyes 2021). Similar to what was found for other high- z quasars and galaxies (e.g., J0100, BRI 1202 QSO, and BRI 1202 SMG), J0305–3150 and the companion galaxy C3 reside on the local star formation law. The molecular gas masses for all the companion galaxies are an order of magnitude lower than those in the quasar.

4.3. The ISM Properties of the Quasar and Its Close Companions

The (sub)millimeter ISM lines and continuum emission provide rich information on the ISM properties. For example, when the illumination radiation field is dominated by X-rays the ISM emission in X-ray dominated regions (XDRs) tends to have a lower $[\text{C II}]_{158 \mu\text{m}}/[\text{C I}]_{369 \mu\text{m}}$ ratio compared to a

radiation field dominated by UV photons (the ISM components illuminated by UV photons are generally referred to as photodissociation regions (PDRs)). In local AGNs and (U) LIRGs, extensive observations of the FIR fine structure lines suggest a deficit of the line-to-FIR ratio with increasing FIR luminosity, namely the “FIR line deficit.” High CO-to-FIR ratios are generally expected when the ISM is heated by, e.g., X-rays or shocks besides UV photons from young massive stars (Uzgil et al. 2016). In this work, we detect the CO, $[\text{C II}]_{158 \mu\text{m}}$, $[\text{C I}]_{369 \mu\text{m}}$, and continuum emissions in the quasar J0305–3150 and its three close companions. Direct comparisons between the quasar and companion galaxies thus enable us to explore the possible impacts of the central accreting supermassive black hole on the ISM.

Adopting a FIR dust continuum modified blackbody model with parameters of $T_{\text{dust}} = 47 \text{ K}$ and $\beta = 1.6$ (Venemans et al. 2019), we calculate the FIR luminosities based on the $[\text{C II}]_{158 \mu\text{m}}$ continuum flux densities for the quasar and the companion galaxies. We obtain CO(6–5)-, CO(7–6)-, $[\text{C I}]_{369 \mu\text{m}}$ - and $[\text{C II}]_{158 \mu\text{m}}$ -to-FIR ratios of 2.3×10^{-5} , 2.3×10^{-5} , 1.4×10^{-5} , and 5.0×10^{-4} for J0305–3150. We adopt dust continuum flux

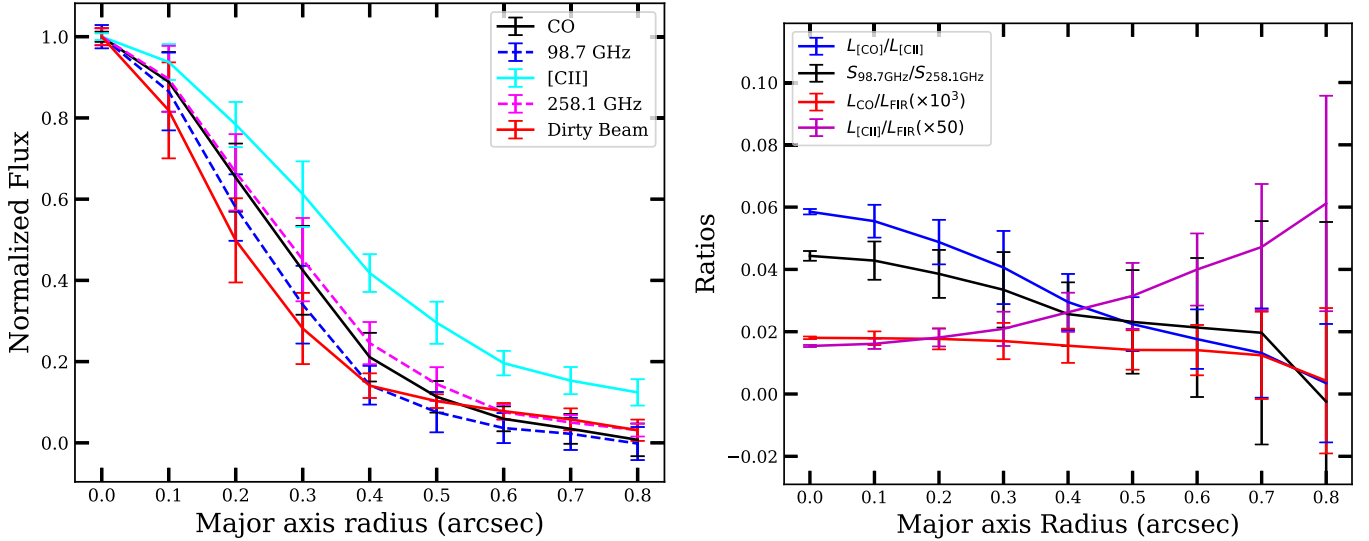


Figure 5. Left: radial profiles of different gas and dust continuum tracers. The line fluxes are normalized to the peak pixel fluxes. Right: same as the left panel, but showing the radio profiles of different line ratios.

densities in Venemans et al. (2020) for FIR luminosity estimations for C1, C2, and C3. We estimate the CO(6–5)-, CO(7–6)-, [C I] $_{369 \mu\text{m}}$, and [C II] $_{158 \mu\text{m}}$ -to-FIR-luminosity ratios for C1 to be $(1.8 \pm 0.5) \times 10^{-5}$, $<1.4 \times 10^{-5}$, $<1.4 \times 10^{-5}$, and $(4.1 \pm 0.9) \times 10^{-3}$. The CO(6–5)-, CO(7–6)-, [C I] $_{369 \mu\text{m}}$, and [C II] $_{158 \mu\text{m}}$ -to-FIR-luminosity ratios of C2 are $<5.3 \times 10^{-5}$, $<5.9 \times 10^{-5}$, $<5.9 \times 10^{-5}$, and $(8.6 \pm 0.3) \times 10^{-4}$. As for C3, the ratios between CO(6–5), CO(7–6), [C I] $_{369 \mu\text{m}}$, [C II] $_{158 \mu\text{m}}$ and FIR luminosity are $(1.8 \pm 0.7) \times 10^{-5}$, $(2.7 \pm 0.7) \times 10^{-5}$, $(1.8 \pm 0.5) \times 10^{-5}$, $<1.9 \times 10^{-5}$, and $(8.3 \pm 0.3) \times 10^{-4}$. We also calculate the TIR (8–1000 μm) surface densities and [C II] $_{158 \mu\text{m}}$ /TIR ratios of the quasar, and its companion galaxies C2 and C3 for a direct comparison with other samples. In Figure 6, we show the [C II] $_{158 \mu\text{m}}$ /TIR versus Σ_{TIR} . Similar to that found for other $z \gtrsim 6$ quasars and companion galaxies, J0305–3150 and its companion galaxies follow the spatially resolved [C II] $_{158 \mu\text{m}}$ deficit trend of local LIRGs (Wagg et al. 2012; Jones et al. 2016; Decarli et al. 2017; Díaz-Santos et al. 2017; Neeleman et al. 2019).

In addition, we calculate the [C II] $_{158 \mu\text{m}}$ /[C I] $_{369 \mu\text{m}}$ ratios of the quasar J0305–3150 and its close companions as diagnostics between PDRs and XDRs. The quasar J0305–3150 exhibits a [C II] $_{158 \mu\text{m}}$ /[C I] $_{369 \mu\text{m}}$ ratio of 49.5, which is consistent with PDRs (Meijerink & Spaans 2005; Meijerink et al. 2007). The lower limits of the [C II] $_{158 \mu\text{m}}$ /[C I] $_{369 \mu\text{m}}$ ratios for C1, C2, and C3 are 36.9, 19.5, and 49.6, respectively, which is also within the ranges for the PDR model prediction. Despite the presence of luminous AGNs, the [C II] $_{158 \mu\text{m}}$ /[C I] $_{369 \mu\text{m}}$ ratio of J0305–3150 excludes the XDR dominance in the ISM excitation of the quasar. J0305–3150 reveals a [C II] $_{158 \mu\text{m}}$ -to-CO ratio of ~ 10 . Comparable ratios are found for the companion galaxies. To summarize, we find no significant differences in the line-to-line and line-to-FIR ratios between J0305–3150 and its companion galaxies.

5. Summary

In this work, we present an analysis of the CO(6–5), CO(7–6), [C I] $_{369 \mu\text{m}}$ lines as well as the dust continuum

emission in the quasar J0305–3150 at $0''.4$ resolution. Some of these lines are also detected in the companion galaxies within 40 kpc from the quasar. We summarize the main results below.

1. We detect CO emission in two of the three companion galaxies. Their respective CO fluxes are an order of magnitude fainter than those observed in the quasar. We derive molecular gas masses and molecular gas mass surface densities for the quasar and companion galaxies from both CO and [C I] $_{369 \mu\text{m}}$ luminosities. The gas mass in the quasar is an order of magnitude higher than that found for companion galaxies. The molecular gas mass surface density of the quasar is at the high end of what is found in local starburst galaxies. The upper limits for the gas mass surface densities of the companion galaxies are comparable to the lowest values found in local starburst galaxies and higher than the lowest values found in local spiral galaxies.
2. We compare the radial profiles of the CO, [C II] $_{158 \mu\text{m}}$, and the dust continuum emission of the quasar. The [C II] $_{158 \mu\text{m}}$ profile is above both the CO and the dust continuum, suggesting a more extended spatial distribution of [C II] $_{158 \mu\text{m}}$ relative to the CO and the dust continuum. CO and dust continuum have similar radial profiles, implying a similar gas component to that traced by the CO and the dust. In addition, we calculate the CO/[C II] $_{158 \mu\text{m}}$, [C II] $_{158 \mu\text{m}}$ -to-FIR, CO-to-FIR, and dust continuum $S_{98.7 \text{ GHz}}/S_{258.1 \text{ GHz}}$ ratio profiles. The CO/[C II] $_{158 \mu\text{m}}$ ratio decreases with increasing radius, confirming the more extended spatial distribution of CO compared to [C II] $_{158 \mu\text{m}}$. The decreasing [C II] $_{158 \mu\text{m}}$ -to-FIR ratio with increasing distance to the center is consistent with high resolution [C II] $_{158 \mu\text{m}}$ observations of other $z \gtrsim 6$ quasars. The CO-to-FIR ratio on the other hand is almost flat with radius. We find a decreasing $S_{98.7 \text{ GHz}}/S_{258.1 \text{ GHz}}$ ratio with increasing radius, which is possibly due to a decrease of dust optical depth with increasing radius.
3. We compare the ISM properties in the quasar and companion galaxies through the [C II] $_{158 \mu\text{m}}$ /[C I] $_{369 \mu\text{m}}$, CO/[C II] $_{158 \mu\text{m}}$, [C II] $_{158 \mu\text{m}}$ -to-FIR, and CO-to-FIR

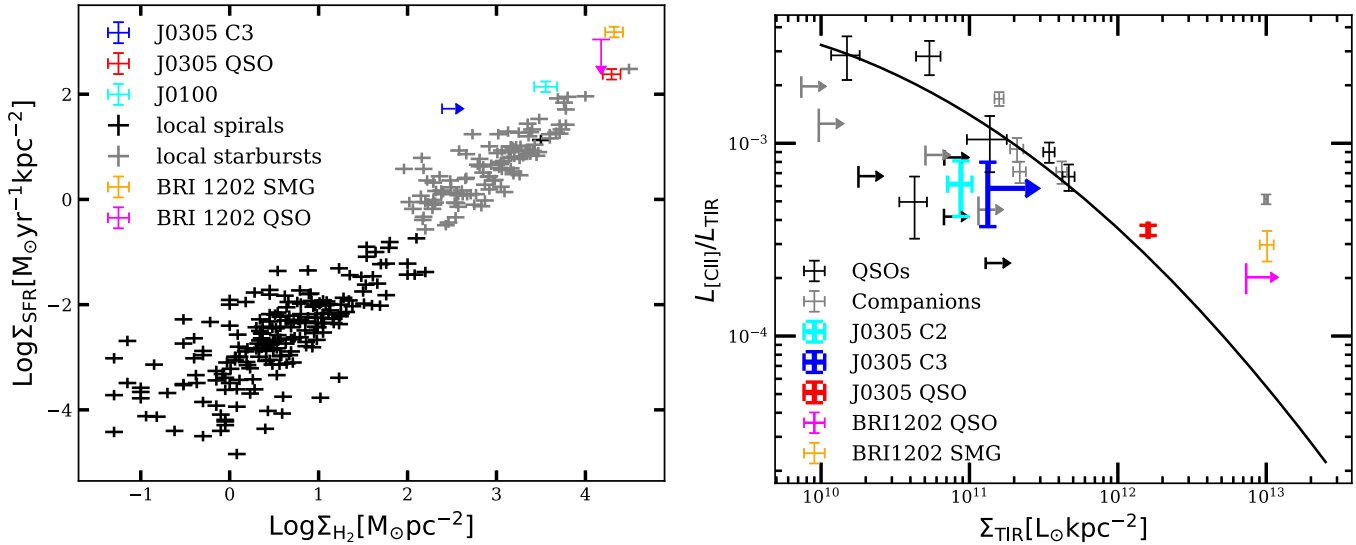


Figure 6. Left: Star formation rate (SFR) surface density vs. molecular gas surface density for J0305–3150 and its companion galaxy C3 (the molecular gas surface densities of C1 and C2 cannot be determined). Comparison samples include local spiral (“local spirals”) and starburst (“local starbursts”) galaxies from de los Reyes & Kennicutt (2019) and Kennicutt & De Los Reyes (2021), the $z = 4.69$ quasar BRI 1202 (“BRI 1202 QSO”) and its companion submillimeter galaxy (“BRI 1202 SMG”) from Wagg et al. (2012) and Jones et al. (2016), and the $z = 6.33$ quasar J0100+2802 (“J0100”) from Wang et al. (2019a). The SFRs of J0305–3150 and C3 are calculated using the same formula as that presented in Kennicutt & De Los Reyes (2021). Right: $[\text{C II}]_{158 \mu\text{m}}$ deficit diagram for the quasar J0305–3150 and its companion galaxies C2 and C3 (C1 is not included because of difficulties in constraining the source size). Assuming the CO lines of C3 to be spatially unresolved, we use the beam size of CO(6–5) as an upper limit for the source size in the total infrared (TIR) surface density estimation of C3. “QSOs” and “companions” refer to $z \sim 6$ quasar and companion galaxy samples collected from Neeleman et al. (2019) and Decarli et al. (2017). The black solid line represents the $[\text{C II}]_{158 \mu\text{m}}$ deficit relation observed in local LIRGs from Díaz-Santos et al. (2017). For the objects in this work and in the comparison samples, the TIR luminosities are estimated from the continuum flux density close to the $[\text{C II}]_{158 \mu\text{m}}$ line frequency through assuming a modified blackbody model with a temperature of 47 K and emissivity of 1.6.

ratios. No significant differences are found between the quasar and the companion galaxies. Future high- J ($J \geq 10$) CO observations will be critical in discriminating the differences of ISM properties between the quasar and the companions.

We thank Mladen Novak and Melanie Kaasinen for their help with the data reduction. We thank the referee for constructive comments that helped improve our manuscript. This work was supported by the National Science Foundation of China (NSFC, 11721303, 11991052) and the National Key R&D Program of China (2016YFA0400703). R.W. acknowledges supports from the NSFC grants No. 12173002, 11533001 and the Thousand Youth Talents Program of China. B.P.V. and F.W. acknowledge funding through ERC Advanced Grant 740246 (Cosmic Gas). This paper makes use of the following ALMA data: ADS/JAO.ALMA#2017.1.01532.S, ADS/JAO.ALMA#2015.1.00399.S. ALMA is a partnership of ESO (representing its member states), NSF (USA), and NINS (Japan), together with NRC (Canada), MOST and ASIAA (Taiwan), and KASI (Republic of Korea), in cooperation with the Republic of Chile. The Joint ALMA Observatory is operated by ESO, AUI/NRAO, and NAOJ.

ORCID iDs

Jianan Li <https://orcid.org/0000-0002-1815-4839>
 Bram P. Venemans <https://orcid.org/0000-0001-9024-8322>
 Fabian Walter <https://orcid.org/0000-0003-4793-7880>
 Roberto Decarli <https://orcid.org/0000-0002-2662-8803>
 Ran Wang <https://orcid.org/0000-0003-4956-5742>
 Zheng Cai <https://orcid.org/0000-0001-8467-6478>

References

- Carilli, C. L., & Walter, F. 2013, *ARA&A*, 51, 105
 de los Reyes, M. A. C., & Kennicutt, R. C. 2019, *ApJ*, 872, 16
 Decarli, R., Walter, F., Venemans, B. P., et al. 2017, *Natur*, 545, 457
 Decarli, R., Walter, F., Venemans, B. P., et al. 2018, *ApJ*, 854, 97
 Díaz-Santos, T., Armus, L., Charmandaris, V., et al. 2017, *ApJ*, 846, 32
 Downes, D., & Solomon, P. M. 1998, *ApJ*, 507, 615
 Jones, G. C., Carilli, C. L., Momjian, E., et al. 2016, *ApJ*, 830, 63
 Kennicutt, R. C., & De Los Reyes, M. A. C. 2021, *ApJ*, 908, 61
 Li, J., Wang, R., Cox, P., et al. 2020a, *ApJ*, 900, 131
 Li, J., Wang, R., Riechers, D., et al. 2020b, *ApJ*, 889, 162
 Mazzucchelli, C., Decarli, R., Farina, E. P., et al. 2019, *ApJ*, 881, 163
 Meijerink, R., & Spaans, M. 2005, *A&A*, 436, 397
 Meijerink, R., Spaans, M., & Israel, F. P. 2007, *A&A*, 461, 793
 Neeleman, M., Bañados, E., Walter, F., et al. 2019, *ApJ*, 882, 10
 Neeleman, M., Novak, M., Venemans, B. P., et al. 2021, *ApJ*, 911, 141
 Novak, M., Bañados, E., Decarli, R., et al. 2019, *ApJ*, 881, 63
 Novak, M., Venemans, B. P., Walter, F., et al. 2020, *ApJ*, 904, 131
 Pensabene, A., Decarli, R., Bañados, E., et al. 2021, *A&A*, 652, A66
 Shao, Y., Wang, R., Carilli, C. L., et al. 2019, *ApJ*, 876, 99
 Shao, Y., Wang, R., Jones, G. C., et al. 2017, *ApJ*, 845, 138
 Uzgil, B. D., Bradford, C. M., Hailey-Dunsheath, S., et al. 2016, *ApJ*, 832, 209
 Venemans, B. P., Decarli, R., Walter, F., et al. 2018, *ApJ*, 866, 159
 Venemans, B. P., Neeleman, M., Walter, F., et al. 2019, *ApJL*, 874, L30
 Venemans, B. P., Walter, F., Decarli, R., et al. 2017, *ApJ*, 845, 154
 Venemans, B. P., Walter, F., Neeleman, M., et al. 2020, *ApJ*, 904, 130
 Wagg, J., Wiklind, T., Carilli, C. L., et al. 2012, *ApJL*, 752, L30
 Walter, F., Riechers, D., Novak, M., et al. 2018, *ApJL*, 869, L22
 Walter, F., Weiß, A., Downes, D., et al. 2011, *ApJ*, 730, 18
 Wang, F., Wang, R., Fan, X., et al. 2019a, *ApJ*, 880, 2
 Wang, R., Shao, Y., Carilli, C. L., et al. 2019b, *ApJ*, 887, 40
 Wang, R., Wagg, J., Carilli, C. L., et al. 2013, *ApJ*, 773, 44
 Wang, R., Wu, X.-B., Neri, R., et al. 2016, *ApJ*, 830, 53
 Weiß, A., Downes, D., Henkel, C., et al. 2005, *A&A*, 429, L25
 Weiß, A., Henkel, C., Downes, D., et al. 2003, *A&A*, 409, L41
 Yang, J., Venemans, B., Wang, F., et al. 2019, *ApJ*, 880, 153